RSC Advances

PAPER

View Article Online
View Journal | View Issue

Cite this: *RSC Adv.*, 2024, **14**, 14194

Electrochemical sensing performance of two CuO nanomaterial-modified dual-working electrodes†

Fengxia Chang, * Dan Wang, Zixian Pu, Jinhang Chen and Jiong Tan

Two CuO nanostructures, namely, nanospheres (CuONSs) and nanochains (CuONCs) with different shapes but similar diameters, were synthesized and characterized. With these two nanomaterials as electrode modifiers, a systematic comparative study was conducted to examine their electrochemical sensing of catechol (CT) using a dual-working electrode system. The results suggest that for CuONS- and CuONC-modified glassy carbon electrodes, the electrode process for the CT redox is diffusion-controlled, and the modification amount and electrolyte pH have a similar effect on the response. However, the CuONCs showed a higher peak current and lower peak potential, as well as a lower detection limit for the electrochemical oxidation of CT. This is explained by the lower charge transfer impedance and higher electroactive surface area of the CuONCs. Notably, an unexpected peak appeared in the cyclic voltammograms when the pH was <4 for the CuONCs and <3 for the CuONSs. For this phenomenon, UV-Vis spectra, zeta potential, and size distribution experiments demonstrated changes in the two CuO nanostructures at lower pH, illustrating that CuONSs can tolerate a higher pH as compared to CuONCs. The multiple comparisons between the two nanomaterials presented here can provide references for the selection of electrochemical sensing materials.

Received 22nd February 2024
Accepted 16th April 2024

DOI: 10.1039/d4ra01356e

rsc.li/rsc-advances

1 Introduction

Copper(II) oxide (CuO) possesses a small energy bandgap and is a worthwhile p-type semiconducting material.[1–3] Because it possesses the traits of high specific capacitance, low cost, easy fabrication and storage, and non-toxicity, it is a versatile material with rich applications in the fields of optics, electrical and photovoltaic components, sensors, catalysts, lithium-ion batteries, and magnetic storage.[4–7]

In recent years, various CuO nanomaterials with different shapes have been studied and applied to electrochemical sensing. For example, CuO nanoparticles have been used to prepare modified carbon paste electrodes, which presented an enhanced response for the detection of dopamine.[8] Significantly lower overpotential was measured for CuO nanowires vertically aligned to a glassy carbon electrode (GCE) in the redox reaction of H_2O_2.[9] Furthermore, a GCE modified with CuO nanochains (CuONCs) assembled with small nanorods showed excellent electrocatalytic activity in nitrite oxidation.[10] Moreover, shuttle-like CuO nanocrystals have been synthesized on a poly(neutral red)-modified GCE, with which the simultaneous detection of adenine and guanine was achieved.[11]

Various CuO-based enzyme-free glucose sensors have been investigated using CuO nanowires, nanosheets, nanoflowers, and rice-like CuO, and these sensors exhibited different sensing performance, for example, limits of detection of 0.049, 0.8, 2.5, and 0.0647 μM, respectively.[12–15] In another report, GCEs were separately modified by CuO nanoparticles, nanoplatelets, and nanorods, and their sensing effects were compared for the nonenzymatic detection of glucose.[16] The electrocatalytic effects of these three CuO nanostructures during the process of glucose oxidation were different, with the order of CuO nanoparticles > CuO nanoplatelets > CuO nanorods. Apparently, not only the sizes but also the structures of CuO nanomaterials substantially influence the electrochemical sensing performance. However, whether the electrocatalytic activity is different for CuO nanospheres (CuONSs) and CuONCs with similar diameters has not been investigated.

The studies comparing sensing performance usually examine redox behaviours with only a group of cyclic voltammograms obtained with electrodes modified by similar nanomaterials, which aim at highlighting the superiority of one of the materials.[16,17] However, the effects of scan rate, modification amount, pH, and voltammetric measurements were not compared. A systematic comparison is necessary for choosing materials to fulfil different needs.

A dual-working electrode system that integrates two different modified electrodes can detect two or more substances in one electrochemical scan. For example, a dual-working electrode system including one graphene oxide-modified GCE and one

School of Chemistry and Environment, Southwest Minzu University, Chengdu, P.R. China. E-mail: changfengxia@swun.edu.cn

† Electronic supplementary information (ESI) available. See DOI: https://doi.org/10.1039/d4ra01356e

glucose oxidase/Prussian blue-graphite-modified GCE was constructed to simultaneously measure uric acid, dopamine, and glucose.[18] Additionally, a bi-aptasensor was demonstrated by separately immobilizing two electrochemical probes on two screen-printed electrodes of a dual-working electrode system for simultaneously determining two tumor markers.[19] The use of dual-working electrodes can achieve multiple detections with one electrochemical scan, which increases detection efficiency. The dual-working electrode system has usually been applied to achieve simultaneous detection of two or more analytes, while a comparative study of the sensing of one analyte between two different modification materials has not yet been conducted using it.

In this work, a systematic comparison of the sensing of two different materials was conducted. Performance indicators, including a scan rate study, effect of modification amount, effect of pH, and voltammetric measurements, as well as redox behaviours, were measured, and for the first time, a dual-working electrode system was applied for the comparison. Specifically, the dual-working electrode system was constructed using CuONSs and CuONCs of similar diameter as the modification materials (Scheme 1). The electrochemical sensing performance of these nanomaterials was studied and compared using catechol (CT) as the analyte. CT is a highly toxic dihydroxybenzene pollutant with strong instability and poor biodegradability, and it is also an important chemical raw material in industry.[20–22] The electrochemical method used for the determination of CT requires advantages such as a simple instrument and experimental process, rapid analysis, easy miniaturization, and on-site detection.[23–27] Moreover, CuO-based nanocomposites such as CuO-carbon nano-fragments, poly(safranine T)-deep eutectic solvent/CuO nanoparticle-carbon nanotube nanocomposite, and CuO/TiO_2 heterojunctions can enhance the electrochemical oxidation and reduction of CT as previously reported.[28–30] However, there have been no previous studies that have simultaneously applied CuONSs and CuONCs for the electrochemical sensing of CT. Therefore, CT was selected for the comparative study, and the performance differences between the CuONS- and CuONC-modified electrodes were investigated in detail using various characterization methods.

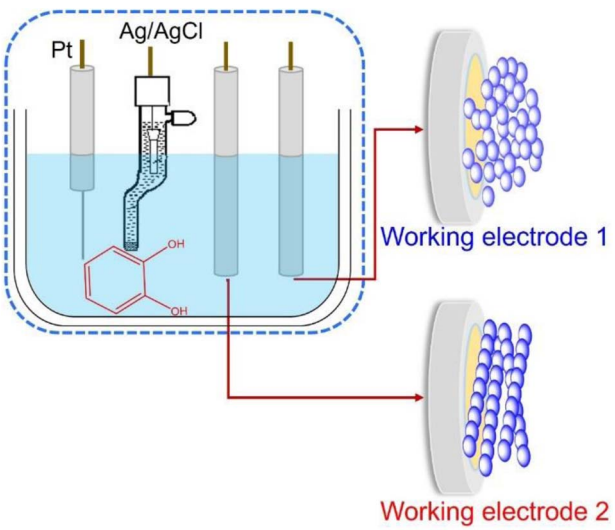

Scheme 1 Diagrammatic sketch of the dual-working electrode system.

2 Experimental

2.1 Chemicals

Chemicals of analytical grade including catechol, $CuSO_4 \cdot 5H_2O$, NaOH, $K_4[Fe(CN)_6]$, KCl, NaH_2PO_4, and Na_2HPO_4, as well as $NH_3 \cdot H_2O$ (500 mg L^{-1} in water) were provided by Kelong (Chengdu, China).

2.2 Equipment

The electrochemistry tests were conducted at a CHI 760E workstation (ChenHua, China). A Talos F200S transmission electron microscope (FEI, USA) and a Merlin Compact scanning electron microscope (Zeiss, Germany) provided the morphology results. Samples for transmission electron microscopy (TEM) were prepared by placing a drop of precipitate (dispersed in water by ultrasonication for 10 min) on a carbon-coated copper grid and allowing it to dry in air. The X-ray diffraction (XRD) measurements were implemented with a D8 Advance diffractometer (Bruker, Germany). The Raman spectra of the CuO nanostructures were recorded on a LabRAM HR Evolution spectrophotometer equipped with an Ar ion 514 nm laser (Horiba, Japan). The X-ray photoelectron spectra (XPS) were recorded on a K-Alpha spectrometer (Thermo, USA). The absorption spectral study was performed using a 1800PC UV-Vis spectroscope (Mapada, China) with a deuterium lamp as the irradiation source and phosphate-buffered saline (PBS) as the reference. A ZEN3690 Zetasizer (Malvern, UK) was applied to measure the zeta potential and size distribution, and the test temperature was 25 °C, the number of cycles was 10, and the dispersant was water.

2.3 Synthesis of CuONSs

The CuONSs were synthesized using a previously reported method, with minor changes.[31] In particular, a 0.1 M $CuSO_4$ solution was mixed dropwise into a 0.2 M NaOH solution, and the suspension containing the precipitate was constantly stirred for 1 h at room temperature. The precipitate was collected by centrifugation and then washed 3 times with ethanol and water in sequence. After drying at 80 °C in an oven for 2 h, the obtained product was placed into a porcelain crucible and then heated to 400 °C for 3 h in a muffle furnace.

2.4 Synthesis of CuONCs

The CuONCs were synthesized following a reported method with minor adjustments.[32] In the synthesis, 2 g of $CuSO_4 \cdot 5H_2O$ was added to 200 mL water, followed by stirring for 1 h. Next, 10 mL of $NH_3 \cdot H_2O$ solution (0.1 M) was rapidly mixed into the $CuSO_4$ solution, along with constant stirring. After that, 2 M NaOH solution was added dropwise, with adjustment of the pH

to approximately 12. The generated blue precipitate was centrifuged and washed with water and ethanol. The product was heated at 100 °C for 10 h in air.

2.5 Electrode preparation

The CuONSs or CuONCs powder was dispersed in water by ultrasound for 10 min to prepare modified suspensions with concentrations of 3 mg mL^{-1}. The GCEs (3 mm) were polished on a flannelette covered by 0.05 mm alumina slurry and ultrasonically rinsed in ethanol and water before use. The CuONS- or CuONC-modified GCEs (CuONSs/GCE or CuONCs/GCE) were fabricated by dropping the corresponding suspension (3 μL) separately onto the working area of the GCE and drying using an infrared lamp.

2.6 Electrochemistry experiments

The electrochemistry experiments were conducted with the solution saturated with ultra-pure N_2. An Ag/AgCl electrode (3 M KCl) and a platinum electrode were employed as the reference and counter electrode, respectively, and the CuONSs/GCE and CuONCs/GCE were set as dual-working electrodes. Cyclic voltammetry (CV) was implemented with CT dissolved in 0.1 M phosphate-buffered saline (PBS, pH 7.0, containing 0.1 M KCl) at a scan rate of 50 mV s^{-1} except for the scan rate study. The linear sweep voltammetry (LSV) diagrams were recorded at 50 mV s^{-1} in CT at different concentrations. All voltammetric scanning was repeated 4 times for each voltammogram. The electrochemical impedance spectroscopy (EIS) and chronocoulometric curves were recorded with CuONSs/GCE and CuONCs/GCE as separate single working electrodes in 5 mM $K_3/K_4[Fe(CN)_6]$ solution containing 0.1 M KCl.

3 Results and discussion

3.1 Nanostructural characterization

The morphology of the as-synthesized CuONSs and CuONCs was provided by scanning electron microscopy (SEM) and TEM. The SEM images of the two nanostructures are displayed in Fig. 1A and B. The CuONSs possess a spherical structure with diameters of approximately 40 nm. In contrast, Fig. 1B displays a chain-like nanostructure with large-scale uniformity for the CuONCs. The mean length of the chains is several micrometers, and they are approximately 40 nm in diameter.

The TEM image of the CuONSs, as displayed in Fig. 1C, shows that their diameters range from 35 to 45 nm, and the high-resolution TEM (HRTEM) image (Fig. 1E) exhibits a lattice distance of 0.252 nm. The TEM image of the as-synthesized CuONCs (Fig. 1D) demonstrates that the nanochains consist of one-dimensionally integrated particles with diameters of approximately 40 nm. The HRTEM image of the CuONCs (Fig. 1F) exhibits a lattice spacing of 0.247 nm.

The XRD characterization results of the CuONSs and CuONCs are presented in Fig. S1.† The peaks of two nanostructures could be ascribed to the monoclinic phase of CuO (JCPDS 89-2530), indicating that the structures dominate and crystallize well. Along with the SEM and TEM results, it was demonstrated that the two CuO nanostructures with similar diameters were successfully synthesized. The Raman spectra showed three peaks corresponding to the A_g (278 cm^{-1}), $B_g{}^1$ (327 cm^{-1}), and $B_g{}^2$ (604 cm^{-1}) modes of the CuONSs, respectively, and these peaks appeared in the Raman spectra of the CuONCs at 277, 321, and 609 cm^{-1}, respectively. The wave number differences might have occurred due to differences in the morphology in the two cases, as shown in the TEM results.

XPS analysis was carried out to investigate the chemical valence state of Cu on the surface of the CuO nanostructures. The fitted Cu 2p spectrum of the two structures showed that the characteristic peaks at the binding energy of 934.9 eV and 954.93 eV were attributed to Cu(II).[33] Also, the peaks at 933.5 eV and 953.4 eV indicated the existence of Cu(I) in the CuONSs and CuONCS.[34]

3.2 Comparison of electrochemical performance in CT redox

3.2.1 CT redox at electrodes modified with CuO nanomaterials. The electrocatalytic effect of the CuONSs or CuONCs on CT redox was studied in 0.5 mM CT dissolved in PBS. Two GCEs were modified by CuONSs and CuONCs, respectively, and were used as dual-working electrodes to maintain consistent detection conditions and high detection efficiency. Fig. 2 shows the cyclic voltammograms (CVs) of CT at the GCEs unmodified and modified with CuONSs or CuONCs. There were oxidation peaks for CT at 0.45 V, with a peak current of 6.41 μA for the two bare GCEs acting as dual-working electrodes. The almost coincident CV curves illustrate the consistency of the two GCEs and the feasibility of the dual-working electrode system.

For the modified dual-working electrodes, an anodic peak appeared at 0.40 V with a peak current of 13.8 μA at the CuONS-modified GCE. At the CuONC-modified GCE, the peak of CT oxidation occurred at 0.36 V, and the peak current was 16.9 μA. Collectively, the anodic peak currents of CT at the CuONS- and CuONC-modified GCEs were 2.2- and 2.6-fold higher than those at the bare GCEs, respectively. Additionally, the anodic peak potentials at the CuONS- and CuONC-modified GCEs were 0.05 V and 0.09 V less than those at the bare GCEs, respectively. To ensure that there are statistically meaningful differences between the electrodes, 4 replicate measurements were conducted, and the relative standard deviation (RSD) of the oxidation peak potential and current (Table S1†) sufficiently proved that these differences were not from error in the measurements.

The higher redox currents and lower oxidation potential of CT at the modified GCEs in contrast to the bare GCEs can be ascribed to the high surface area and satisfactory crystallinity, as well as satisfactory dimensional uniformity of the CuO nanostructures, which increased the electrocatalytic active sites and improved the electron transfer as a result. Regarding the comparison of these two CuO nanomaterials, the CuONCs showed lower oxidation potential with higher anodic peak current, suggesting higher electrocatalytic activity for CT oxidation as compared to the CuONSs. To explain this phenomenon, investigations with greater detail were conducted, as described in Section 3.3.1.

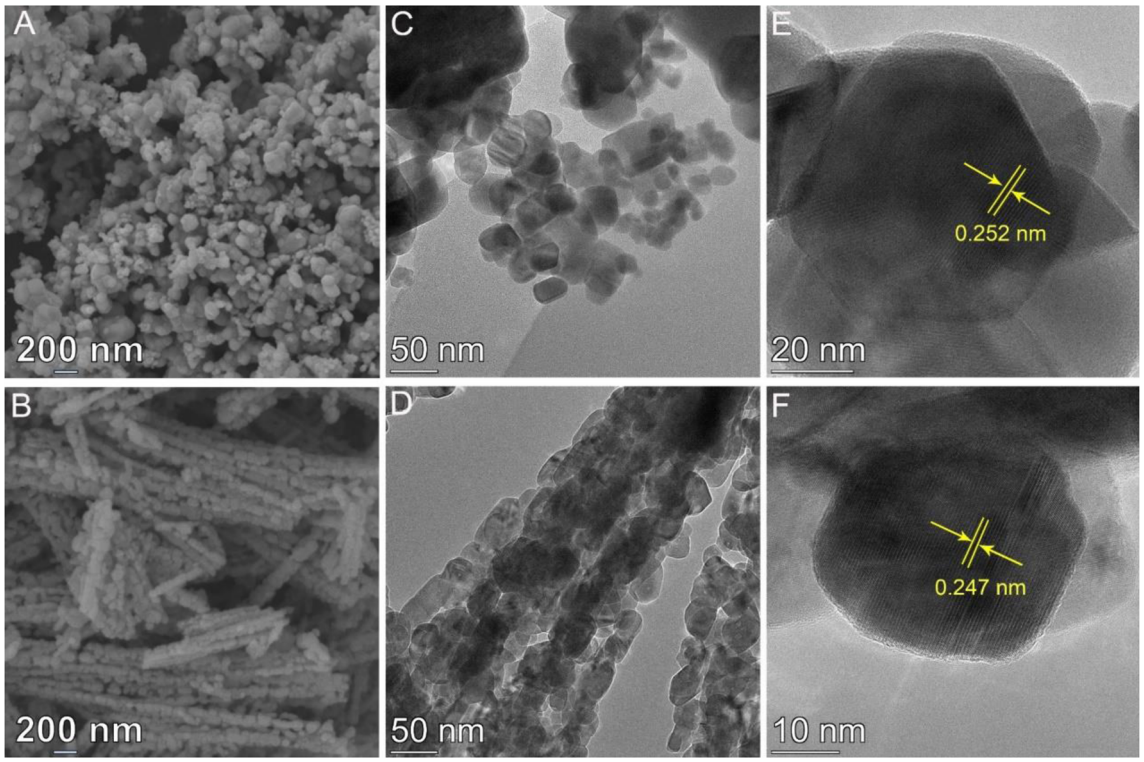

Fig. 1 SEM, TEM, and HRTEM images of (A, C, E) CuONSs and (B, D, F) CuONCs.

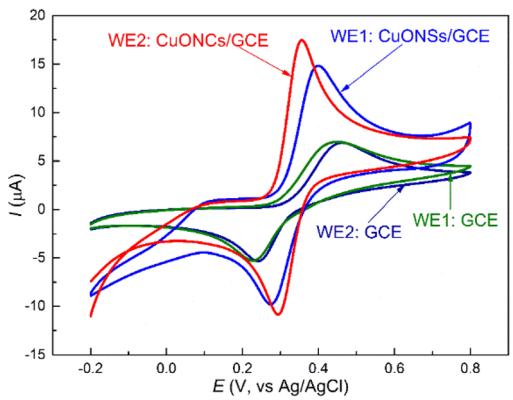

Fig. 2 CV results for 0.5 mM CT in PBS (pH 7.0) at unmodified GCE, CuONSs/GCE, and CuONCs/GCE. Scan rate: 50 mV s^{-1}.

3.2.2 Study of the scan rate. The electrochemical redox of CT at an unmodified GCE is diffusion-controlled (Fig. S2†). To determine whether it was diffusion- or adsorption-controlled at the CuO nanostructure-modified GCEs, CV scans were implemented at various scan rates with dual-working electrodes composed of CuONSs/GCE and CuONCs/GCE. The voltammograms (Fig. 3A and B) show enhanced peak currents for CT with increasing scan rate. The relationships between the oxidation/reduction peak current and the square root of the scan rate are linear, and the related coefficients are 0.999/0.999 and 0.998/0.999 for the CuONS- and CuONC-modified GCEs, respectively (Fig. 3C). Thus, the redox processes of CT at the CuONS- and CuONC-modified electrodes were also diffusion-controlled.

3.2.3 Effect of the modification amount. The modification amounts of CuONSs and CuONCs on the electrode surfaces were optimized for a higher response of CT using the dual-working electrode system. As the CV results obtained using different volumes of modification suspension (Fig. S3†) shown, the peak currents were enhanced by increasing the modification volume from 2 to 3 μL, while a larger volume resulted in a lower peak current. The optimal modification amounts were the same for CuONSs/GCE and CuONCs/GCE. Therefore, a 3 μL modification suspension was used in all subsequent experiments.

3.2.4 Effect of pH. Because the proton participates in the CT redox, there is an important influence by solution pH on the electrode response process. The pH effect was investigated and compared for the CuONS- and CuONC-modified GCEs. CVs were recorded over pH values varying from 8.0 to 3.0 with the dual-working electrode system. As shown in Fig. 4, the redox peaks appear at reduced potentials with increasing pH for the CuONS- and CuONC-modified GCEs. At pH 7.0, the oxidative peak current was highest for both modified electrodes. Therefore, the CT solutions in the subsequent experiments were prepared with PBS at pH 7.0. Unexpectedly, an unknown peak appeared in the anodic curve to the left of the oxidation peak of CT at a lower pH at the CuO nanostructure-modified GCE, and no additional peaks were observed with an unmodified GCE, as presented in Fig. S4.† For the CuONS-modified GCE, the peak appeared at pH 3.0. In contrast, for the CuONC-modified GCE, the peak began to appear at pH 4.0. To investigate the reason for

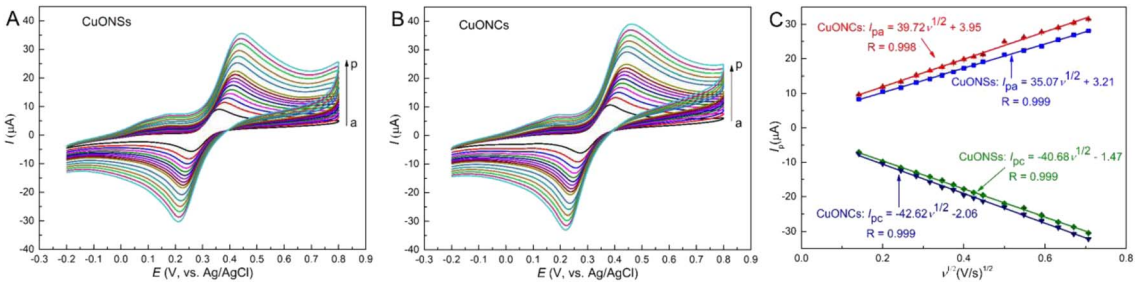

Fig. 3 CVs of 0.5 mM CT in PBS (pH 7.0) for (A) CuONSs/GCE and (B) CuONCs/GCE at different scan rates (a–p: 20, 40, 60, 80, 100, 120, 140, 160, 180, 200, 250, 300, 350, 400, 450, and 500 mV s^{-1}). (C) Linear diagrams of redox peak currents with $\nu^{1/2}$.

these unexpected peaks, further characterization was carried out, as described in Section 3.3.2.

Additionally, the oxidation peak potentials (E_{pa}) of CT at the two modified electrodes negatively shifted as the pH increased, and showed a linear relationship with pH, as presented in Fig. 4C. The results demonstrate that protons directly take part in the reactions, and according to the Nernst equation:

$$\frac{dE_{pa}}{dpH} = \frac{2.303mRT}{nF} \quad (1)$$

the ratio of the proton number (m in the equation) and electron number (n in the equation) was calculated to be 0.981 and 0.998 for the CuONS- and CuONC-modified GCEs, respectively. The results indicate that the oxidation of CT at the two electrodes involves transferring equal numbers of protons and electrons, and the mechanism of the reaction is in accordance with previous reports.[35,36]

3.2.5 Voltammetric measurements for CT. The LSV technique was applied to measure different concentrations of CT using the CuONS- and CuONC-modified GCEs as dual-working electrodes. Fig. 5 depicts the LSV curves and corresponding calibration curves. At the CuONS-modified GCE, the peak current is linear against a concentration range of 0.002–1 mM, with the fitted equation being I_{pa} (μA) = 21.09C (mM) + 1.57 (R = 0.998). At the CuONC-modified GCE, the fitted equation is I_{pa} (μA) = 36.65C (mM) + 2.75 (R = 0.998) in the range of 0.001–1 mM. The limits of detection were estimated to be 0.57 and 0.29 μM (S/N = 3) at the CuONS- and CuONC-modified electrodes, respectively. Apparently, there was a wider linear response range and lower detection limit for the CuONC-modified GCE.

3.2.6 Selectivity and stability study. Several interfering substances were added to the CT solution to examine the selectivity of the CuONS- and CuONC-modified GCEs (Fig. S5A†). The peak currents obtained with LSV showed that a 10-fold concentration of Mg^{2+}, Ca^{2+}, Zn^{2+}, SO_4^{2-}, NO_3^-, phenol, resorcinol, and hydroquinone resulted in no observable influence on the CT signal. These results indicate that a satisfying selectivity of the two electrodes exists for CT.

The overtime stability was tested *via* intermittently measuring the CT solution (every two days) with the modified electrodes stored in the refrigerator (4 °C). The CuONS- and CuONC-modified GCEs maintained approximately 94% and 92%, respectively, of the original peak current after 14 days (Fig. S5B†), which demonstrated satisfactory stability of the electrodes.

3.2.7 Sample detection. Tap water and lake water samples were measured with the CuONS- and CuONC-modified GCEs, and the recovery study was performed with CT added to the samples. The recovery rates with the two electrodes (Table S2†) are within a reasonable range, and no significant difference appeared between them.

3.3 Investigation on the cause of the performance differences

3.3.1 Electrochemical characterization. The electroactive surface area (ESA) of the CuONS- and CuONC-modified GCEs was estimated *via* the chronocoulometric method with

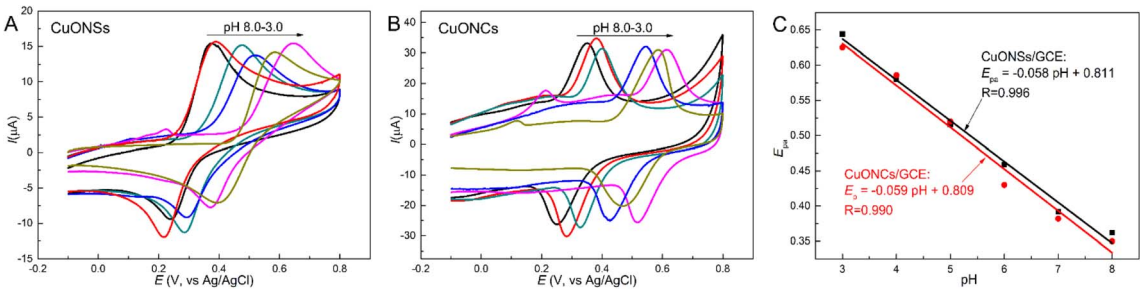

Fig. 4 CV results for 0.5 mM CT in 0.1 M PBS at different pH values (from left to right: 8.0, 7.0, 6.0, 5.0, 4.0, 3.0) for (A) CuONSs/GCE and (B) CuONCs/GCE. Scan rate: 50 mV s^{-1}. (C) Linear relationship curves of oxidation peak potential with pH.

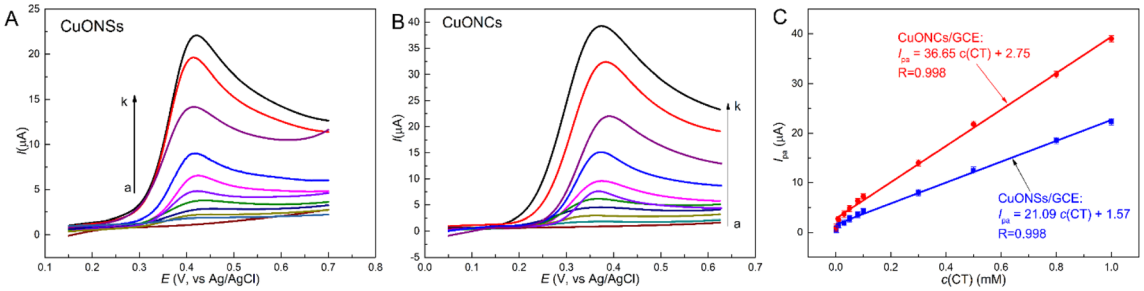

Fig. 5 LSV results for (A) CuONSs/GCE and (B) CuONCs/GCE in 0.1 M PBS (pH 7.0) containing CT at (A) (a) 0 mM, (b) 0.002 mM. (B) 0.001 mM, (c) 0.01 mM, (d) 0.03 mM, (e) 0.05 mM, (f) 0.08 mM, (g) 0.1 mM, (h) 0.3 mM, (i) 0.5 mM, (j) 0.8 mM, (k) 1 mM. Scan rate: 50 mV s^{-1}. (C) Linear plots of peak current *vs.* concentration (4 measurements per point).

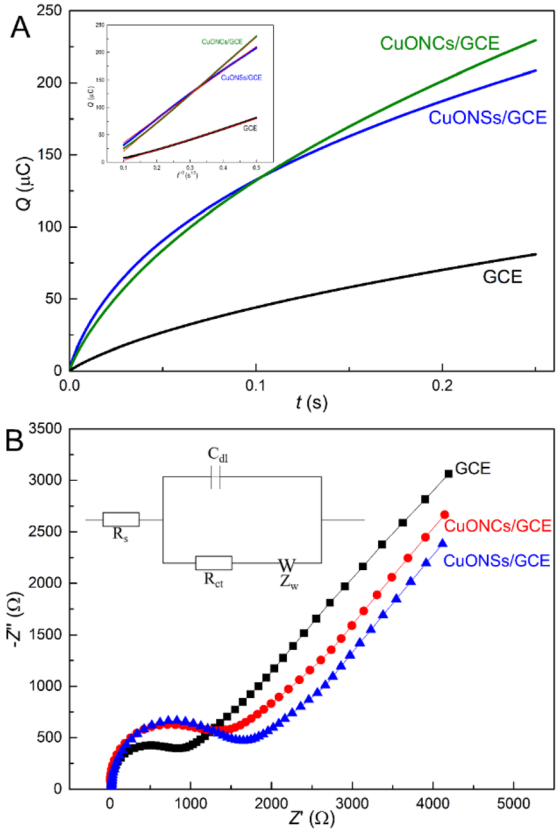

Fig. 6 (A) Chronocoulometric curves and (B) Nyquist diagrams (0.01 Hz to 100 kHz) for GCE, CuONSs/GCE, and CuONCs/GCE in 5 mM $K_3/K_4[Fe(CN)_6]$ containing 0.1 M KCl. The inset of (A) shows Q–$t^{1/2}$ plots.

$[Fe(CN)_6]^{3-/4-}$ as the redox probe (Fig. 6A). The ESA was computed using:[37]

$$A = a/2nFCD^{1/2}\pi^{1/2} \quad (2)$$

where A denotes the ESA (cm^2), a denotes the slope of the charge–$t^{1/2}$ curve (C $s^{-1/2}$), n denotes the number of electrons involved, F denotes Faraday's constant (C mol^{-1}), C denotes the concentration of the redox probe (mol mL^{-1}), and D denotes the probe diffusion coefficient (6.2×10^{-6} cm^2 s^{-1}). The ESAs of the unmodified GCE and GCEs modified by CuONSs and CuONCs are equal to 0.0447, 0.103, and 0.122 cm^2 by calculation, respectively, demonstrating higher ESAs for both modified electrodes compared with the unmodified GCEs. The CuONC-modified GCE showed the highest ESA between the two modified electrodes.

EIS was carried out for further electrochemical characterization. In the mid- to high-frequency semicircular region of a Nyquist diagram, the impedance corresponding to the electrochemical transfer resistance is triggered by the electrochemical reaction at the interface between the electrode and the electrolyte. A lower *R*ct value indicates less electrochemical transfer resistance in the material. Fig. 6B shows the Nyquist diagrams of the unmodified GCE and GCEs modified with CuONSs and CuONCs (0.01 Hz to 100 kHz). Fitted using the Randles circuit model, the *R*ct values for the unmodified GCE and GCEs modified by CuONSs and CuONCs were estimated to be 0.81, 1.42, and 1.26 kΩ, respectively (Table S3†). It is clear that after being modified with the CuO nanomaterials on the GCE, the electrochemical impedance increases, indicating adsorption of the CuO nanomaterials on the electrode surface. The electrochemical transfer resistance of the CuONC-modified electrode is lower than that of the CuONS-modified electrode, which could lead to a higher electrochemical response at the CuONC-modified electrode.

It can be concluded from the above characterization that the CuONC-modified GCE benefited from a higher ESA and lower electrochemical transfer impedance compared with the CuONS-modified GCE, and therefore, the CT determination performance was more robust.

3.3.2 UV-Vis absorption, zeta potential, and size distribution characterization. To investigate the origin of the unexpected peaks in the CVs at low pH (Fig. 4), the UV-Vis spectra, zeta potential, and size distribution of the CuONSs and CuONCs at different pH values were recorded. The UV-Vis spectrum of the CuONSs dispersed in PBS at pH 6.0 shows two weak absorption peaks at approximately 293 and 275 nm, which correspond to the d–d transition and the band-to-band transition for CuO (Fig. 7A).[38] At pH 5.0 and 4.0, the absorption spectra of the CuONSs are similar to that at pH 6.0. However, when the CuONSs were dispersed in PBS at pH 3.0, a strong absorption band at approximately 214 nm appeared in addition

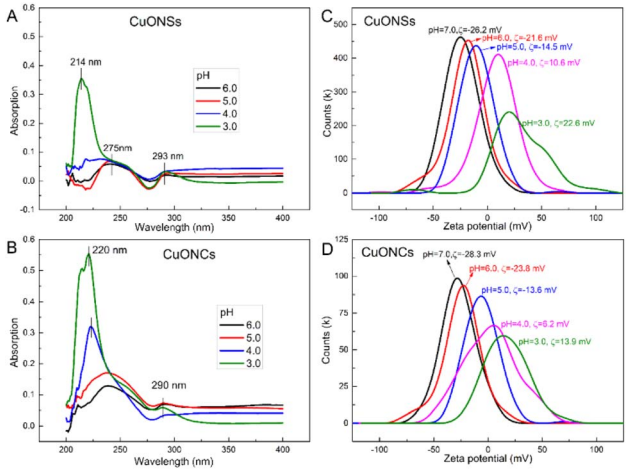

Fig. 7 Absorption spectra and zeta potential of (A, C) CuONSs and (B, D) CuONCs dispersed in PBS at different pH values.

to a shoulder peak at approximately 275 nm and a weak band at approximately 293 nm.

Apparently, the properties of the CuONSs changed when the pH decreased to 3.0. In contrast, for the CuONCs, the changes occurred at a higher pH, because the significant changes in the absorption spectra appeared at pH 4.0 (Fig. 7B). In particular, the spectra of the CuONCs at pH 6.0 and 5.0 exhibited two weak peaks at approximately 290 and 275 nm, and a strong band at approximately 220 nm appeared when the pH was 4.0, which strengthened further as the pH decreased to 3.0. The appearance of the additional peaks in the UV spectra of CuONSs and CuONCs when the pH decreased might have been caused by the change in the morphology, which resulted in increased defects on the CuO nanocrystals, and for CuONCs, the changes occurred at higher pH values.[32]

The zeta potential refers to the potential of the shear plane and is also known as the electromotive potential or electromotive force. It is a key index of the stability of particle dispersion systems. The aqueous media, including pH, can affect the zeta potential, because it varies depending on the ionic composition in the media. The zeta potentials of the CuONSs and CuONCs at different pH values were measured, and are displayed in Fig. 7C and D, respectively. The zeta potentials increased with decreasing pH for the two CuO nanostructures. For the CuONSs, the curves varied, and a notable change in the form of a lower and wider peak appeared at pH 3.0. In contrast, for the CuONCs, the curves became lower and wider as the pH decreased to pH 4.0. Furthermore, although the lowest absolute value of zeta potential appeared at pH 4.0 for both CuO nanostructures, it was higher for the CuONSs as compared with the CuONCs, indicating higher stability. Therefore, it can be concluded that the tolerance of low pH by CuONSs was greater as compared with the CuONCs.

The size distributions of the two CuO nanostructures were determined at pH 7.0 and the lower pH at which the unexpected voltammogram peaks appeared (Fig. S6†). It was found that the size of the CuONCs decreased, and the size distribution became significantly broader at pH 4.0 compared with that at pH 7.0. For the CuONSs, the change was not as obvious as for the CuONCs, even at pH 3.0. Along with the results of the UV-Vis spectral and zeta potential analyses, it can be deduced that the surface of the two CuO nanostructures dissolved at a lower pH, and a greater amount of internal defects was exposed, which may lead to the oxidation of Cu(I) to Cu(II) and generate the unexpected peaks in the CV measurement. From the comprehensive results above, it can be concluded that the CuONSs maintained stability until the pH decreased to 3.0, while the CuONCs were able to perform well at pH > 4.0. Therefore, the pH tolerance of the CuONSs was greater when compared to the CuONCs, which is an important factor when choosing a modifier.

4 Conclusions

Two different CuO nanostructures (CuONSs and CuONCs) with similar diameters were synthesized and characterized. The two nanomaterials were used as electrode modifiers for the electrochemical sensing of CT, and a dual-working electrode was employed for the comparison of the sensing performance. Both sensors exhibited enhanced electrocatalysis in the CT redox reaction, and the comparative results indicated that there was a higher current and lower potential for the CuONCs, as well as a lower detection limit for the oxidation of CT. This could be due to the lower charge transfer impedance and higher electroactive surface area of the CuONCs. Additionally, the electrode process for CT redox was diffusion-controlled for the CuONS- and CuONC-modified GCEs, and the response was similarly affected by the modification amount and electrolyte pH.

Based on the cyclic voltammograms from the study of the pH effect, UV-Vis spectra, zeta potential, and size distribution results, it was demonstrated that the pH tolerance of the CuONSs was stronger when compared with that of the CuONCs. Therefore, these two materials can be selected according to different determination conditions and requirements.

Conflicts of interest

There are no conflicts to declare.

Acknowledgements

The support from the Fundamental Research Funds for the Central Universities (Southwest Minzu University, No. ZYN2023020) and Sichuan Science and Technology Program (No. 2023NSFSC1132) is indebtedly acknowledged.

References

1 M. Khalaj, M. Kamali, Z. Khodaparast and A. Jahanshahi, *Ecotoxicol. Environ. Saf.*, 2018, **148**, 813–824.
2 J. Zhang, J. Liu, Q. Peng, X. Wang and Y. Li, *Chem. Mater.*, 2006, **18**, 867–871.

3 S. H. Weng, Y. J. Zheng, C. F. Zhao, J. Z. Zhou, L. Q. Lin, Z. F. Zheng and X. H. Lin, *Microchim. Acta*, 2013, **180**, 371–378.
4 A. Umar, M. M. Rahman, A. Al-Hajry and Y. B. Hahn, *Electrochem. Commun.*, 2009, **11**, 278–281.
5 T. Shalaby, H. Hamad, E. Ibrahim, O. Mahmoud and A. Al-Oufy, *Ecotoxicol. Environ. Saf.*, 2018, **162**, 354–364.
6 N. Alahmadi, H. S. Alhasan, H. Gomaa, A. A. Abdelwahab and M. Y. Emran, *Microchem. J.*, 2022, **183**, 107909.
7 M. M. Li, X. Y. Peng, Z. G. Liu, Y. Dai, Y. J. Han, L. F. Fan and Y. J. Guo, *Analyst*, 2023, **148**, 2709–2716.
8 S. Reddy, B. E. K. Swamy and H. Jayadevappa, *Electrochim. Acta*, 2012, **61**, 78–86.
9 W. Jia, M. Guo, Z. Zheng, T. Yu, Y. Wang, E. G. Rodriguez and Y. Lei, *Electroanalysis*, 2008, **20**, 2153–2157.
10 C. Xia, X. L. Cai, W. Ning and G. Lin, *Anal. Chim. Acta*, 2011, **691**, 43–47.
11 X. Liang, X. Y. Zhang, F. W. Wang, M. Xu and X. Bao, *J. Solid State Electrochem.*, 2014, **18**, 3453–3461.
12 Z. J. Zhuang, X. D. Su, H. Y. Yuan, Q. Sun, D. Xiao and M. M. F. Choi, *Analyst*, 2008, **133**, 126–132.
13 L. L. Tian and B. T. Liu, *Appl. Surf. Sci.*, 2013, **283**, 947–953.
14 S. G. Leonardi, S. Marini, C. Espro, A. Bonavita, S. Galvagno and G. Neri, *Microchim. Acta*, 2017, **184**, 2375–2385.
15 M. Deng, Q. Jiang, Z. H. Duan, Q. Q. Liu, L. Jiang and X. Y. Lu, *J. Inorg. Mater.*, 2019, **34**, 152–158.
16 F. Y. Huang, Y. M. Zhong, J. Chen, S. X. Li, Y. C. Li, F. Wang and S. Q. Feng, *Anal. Methods*, 2013, **5**, 3050–3055.
17 A. Ajith and S. A. John, *Electrochim. Acta*, 2022, **426**, 140830.
18 A. Soleh, P. Kanatharana, P. Thavarungkul and W. Limbut, *Microchem. J.*, 2020, **153**, 104379.
19 M. A. Tabrizi, M. Shamsipur, R. Saber and S. Sarkar, *Sens. Actuators, B*, 2017, **240**, 1174–1181.
20 X. B. Liu, F. Y. He, L. W. Bai, X. W. Cao, C. Liu and W. B. Lu, *Anal. Chim. Acta*, 2022, **1210**, 339871.
21 Z. W. Lu, K. Wei, H. Ma, R. T. Duan, M. M. Sun, P. Zou, J. J. Yin, X. X. Wang, Y. Y. Wang, C. Wu, G. H. Su, M. J. Wu, X. G. Zhou, J. S. Ye and H. B. Rao, *Anal. Chim. Acta*, 2023, **1251**, 340983.
22 J. S. A. Nair, S. Saisree and K. Y. Sandhya, *Analyst*, 2022, **147**, 2966–2979.
23 R. M. Huang, S. S. Chen, J. G. Yu and X. Y. Jiang, *Ecotoxicol. Environ. Saf.*, 2019, **184**, 109619.
24 C. Wu, Q. Cheng and K. B. Wu, *Anal. Chem.*, 2015, **87**, 3294–3299.
25 J. Li, J. F. Xia, F. F. Zhang, Z. H. Wang and Q. Y. Liu, *Talanta*, 2018, **181**, 80–86.
26 X. Y. Wang, M. Xi, M. M. Guo, F. M. Sheng, G. Xiao, S. Wu, S. Uchiyama and H. Matsuura, *Analyst*, 2016, **141**, 1077–1082.
27 F. G. Wu, J. Zhao, D. X. Han, S. F. Zhao, R. Zhu and G. F. Cui, *Analyst*, 2021, **146**, 232–243.
28 L. A. Alshahrani, L. Y. Liu, P. Sathishkumar, J. M. Nan and F. L. Gu, *J. Electroanal. Chem.*, 2018, **815**, 68–75.
29 B. Dalkiran and C. M. A. Brett, *Microchem. J.*, 2022, **179**, 107531.
30 D. Manoj, S. Rajendran, M. Naushad, M. Santhamoorthy, F. Gracia, M. S. Moscoso and M. A. Gracia-Pinilla, *Environ. Res.*, 2023, **216**, 114428.
31 N. Teymoori, J. B. Raoof, M. A. Khalilzadeh and R. Ojani, *J. Iran. Chem. Soc.*, 2018, **15**, 2271–2279.
32 U. K. Gaur, A. Kumar and G. D. Varma, *CrystEngComm*, 2014, **16**, 3005–3014.
33 A. Y. Kim, M. K. Kim, K. Cho, J. Y. Woo, Y. Lee, S. H. Han, D. Byun, W. Choi and J. K. Lee, *ACS Appl. Mater. Interfaces*, 2016, **8**, 19514–19523.
34 S. Momeni and F. Sedaghati, *Microchem. J.*, 2018, **143**, 64–71.
35 L. Z. Zheng, L. Y. Xiong, Y. D. Li, J. P. Xu, X. W. Kang, Z. J. Zou, S. M. Yang and J. Xia, *Sens. Actuators, B*, 2013, **177**, 344–349.
36 M. Deng, S. R. Lin, X. J Bo and L. P. Guo, *Talanta*, 2017, **174**, 527–538.
37 M. M. Islam and R. Kant, *Electrochim. Acta*, 2011, **56**, 4467–4474.
38 Z. Parsaee, E. J. Bahaderani and A. Afandak, *Ultrason. Sonochem.*, 2018, **40**, 629–643.